

Wake Alleviation Properties of Triangular-Flapped Wings

J. M. Ortega,* R. L. Bristol,* and Ö. Savaş†

University of California at Berkeley, Berkeley, California 94720-1740

The wake alleviation properties of wings with outboard, triangular flap extensions are estimated using data from particle image velocimetry. The experiments are conducted in a towing tank at chord-based Reynolds numbers of $O(10^5)$. The triangular-flapped wings generate two unequal strength, counter-rotating vortex pairs that have circulation strength ratios ranging from -0.4 to -0.7 . Introducing the oppositely signed flap vortices near the tip vortices causes a rapidly growing instability to occur between the vortices on either side of the wake. The resulting nonlinear interactions between the vortices result in a wake that is highly three-dimensional and incoherent. These effects are reflected in a marked decrease in both the rolling moment and downwash on a simulated following wing. To determine the wake alleviation properties of the triangular-flapped wings, their wakes are compared to that of a conventional, rectangular wing. For all of the experimental runs, the wakes of the triangular-flapped wings have maximum rolling moments and downwashes that are substantially less than those of the rectangular wing. The results indicate that the instability in the wake of the triangular-flapped wings offers a possible mechanism to reduce significantly the wake hazard problem.

I. Introduction

AN airplane flying in the vortex wake of another airplane can experience motions anywhere from sudden upwash to downwash to rolling, depending on the airplane's position and orientation with respect to the wake. Near the ground this can be especially dangerous, as the pilot has less time to recover from rapid changes in the airplane's attitude. This hazard is further intensified at airports, where airplanes are continually landing and taking off in the vortex wakes of other airplanes. To deal with the vortex wake hazard, the Federal Aviation Administration in the U.S. and Civil Aviation Authority in Europe regulate the separation distances between successive airline flights, which presumably allows the following aircraft to avoid the hazard caused by the previously generated vortices. To account for the varying behavior of the vortices under different atmospheric conditions, these separation distances are often overly conservative, resulting in unnecessary flight delays and the associated frustrations and costs to the public. Consequently, there is an increasing need to develop a means of tracking or eliminating the trailing vortex hazard. Unfortunately, the technology to track precisely or predict the location of the vortices under all weather conditions is currently unavailable. As a result, a considerable amount of research has been directed toward eliminating the trailing vortex hazard by modifying the airplane that generates them.

In the 1970s NASA tested numerous concepts and devices that were intended to alleviate the wake hazard. Some of these designs, such as splines or wing-tip mounted engines, were intended to force large amounts of turbulence into the vortices.¹⁻⁴ The idea was that the additional turbulence would cause the vortices to dissipate more quickly. Other concepts functioned by modifying the lift distribution of the wing in order to achieve a safer wake. Rossow describes two such lift distributions: a saw-tooth wing loading and a tailored wing loading.⁵ Active wake alleviation designs included such concepts as small, pulsatile jets located at the wing tips and spoilers or flaps that were periodically deployed in flight.² These designs were intended to excite the Crow instability and rapidly cause the linking of the

oppositely signed tip vortices. Passive designs included wing-tip fences, control vortices, and wing-tip turning vanes.^{2,3} In spite of the large number of designs that were tested, none of them were implemented as a solution to wake hazard problem. Simply put, some of the concepts did not effectively reduce the wake hazard, and for those that did the price in airplane performance was too great to make them practical.

More recently, a few concepts have emerged as potential means to control the vortex wake. In 2000, The Boeing Company went public with a design that actively eliminates the wake hazard. By periodically oscillating the outer ailerons and spoilers, an instability is driven, which causes the vortices to form vortex rings rapidly. A similar idea was also demonstrated in numerical simulations of Rennich and Lele.⁶ Another concept for reducing the intensity of wake vortices is based upon an application for military submarines. The research of Quackenbush et al. over the past few years has been directed toward an idea called "vortex leveraging."⁷⁻¹⁰ This concept works by placing shape memory alloy control surfaces on the submarine's sailplanes and periodically oscillating them. The modulated control vortices generated by these surfaces interact with the sailplane vortices, causing an instability to rapidly occur. Though several numerical simulations have been presented, experimental verification does not appear to be available in the open literature.

Another concept is the topic of the present work. Although the trailing vortices cannot be eliminated, they can be forced to lose their coherence by rendering the wake three-dimensional. As noted by Rossow, the acceleration of three-dimensional instabilities is the only viable means for effective wake alleviation.¹¹ As long as the vortices remain parallel, they behave in a nearly two-dimensional fashion, which takes a relatively long time to decay. A robust means to bring about rapid changes in the wake is to utilize passive control vortices. The control vortices can be generated to have a strength comparable to that of the tip vortices, allowing them to alter the behavior of the tip vortices effectively. This was observed in previous towing tank studies, which investigated the merger characteristics of corotating vortex pairs in the wakes of airfoils.^{12,13} By introducing flap vortices near the tip vortices, the trajectories of the tip vortices were altered so that they no longer descended in a near vertical manner, but orbited about the flap vortices in a helical fashion until the vortices merged. Because the merged vortices were just as coherent as the original flap and tip vortices, there was not much reduction in the wake hazard. In considering these results, the question then arose as to what would happen if oppositely signed control vortices were utilized instead? Perhaps by placing these control vortices close to the tip vortices an instability between them would occur, transforming the two-dimensional nature of the wake into a three-dimensional

Received 19 May 2001; revision received 8 November 2001; accepted for publication 21 November 2001. Copyright © 2001 by the American Institute of Aeronautics and Astronautics, Inc. All rights reserved. Copies of this paper may be made for personal or internal use, on condition that the copier pay the \$10.00 per-copy fee to the Copyright Clearance Center, Inc., 222 Rosewood Drive, Danvers, MA 01923; include the code 0001-1452/02 \$10.00 in correspondence with the CCC.

*Graduate Student, Department of Mechanical Engineering. Member AIAA.

†Professor, Department of Mechanical Engineering; savas@me.berkeley.edu. Associate Fellow AIAA.

one. Furthermore, the passive nature of such a concept would make it simple to design and test. An earlier analytical study on the possible behavior of such a multiple vortex system had been made by Donaldson and Bilanin,¹⁴ and Bilanin et al.¹⁵ had studied the wake of a similar type of wing. However, the short wind-tunnel test section used in Bilanin et al.¹⁵ prevented the measurements from being made sufficiently far in the wake of the wing, where the desired effects take place.

To investigate the preceding idea, flow-visualization experiments were done in the wake of a wing with outboard triangular flaps.¹⁶ The results of these experiments revealed that the two, counter-rotating flap/tip vortex pairs undergo a rapidly growing instability within 15–20 spans downstream of the wing. Following this initial set of experiments, more refined flow-visualization measurements were done, allowing further investigation of the instability wavelengths and nonlinear behavior of the vortices.^{17,18} These observations revealed that the sinuous mode along the weaker flap vortices has a wavelength that is on the order of one wingspan (Fig. 1). For runs with smaller circulation strength ratios, the nonlinear effects of the instability lead to a lateral exchange of vorticity across the wing centerline within 50 spans. This exchange occurs when vortex loops from one side of the wake pinch off into rings and advect themselves across the wake. For vortex pairs with slightly larger

circulation strength ratios, the nonlinear effects of the instability remain confined on either side of the wake, as the vortex hoops and rings are flung vertically above the elevation of the wing. Particle image velocimetry (PIV) measurements were made to quantify the relative strengths of the vortices, their trajectories, and the subsequent spreading of vorticity during their interactions. Analysis of the PIV data showed that the two-dimensional kinetic energy drops significantly as the instability transforms the two-dimensional nature of the wake into a three-dimensional one.

Because the distance between the counter-rotating flap/tip pairs is several times greater than the distance between the flap and tip vortices within each pair, the stability characteristics of the vortices in the wake of the triangular-flapped wing can be well approximated by those of a single vortex pair. Theoretical explanations for this instability of a single vortex pair are presented in Bristol et al.¹⁹ In a manner similar to that of Widnall et al.,²⁰ Bristol et al.¹⁹ showed that each vortex in the flap/tip pair imparts a straining field on the other vortex, causing sinuous disturbances to grow. The wavelength of maximum instability is the one in which the vortex self-induced rotation rate keeps the sinuous disturbance aligned in the straining field of the other vortex. Unlike the case of an equal-strength, counter-rotating tip/tip pair,^{20,21} which has a base state of simple descent, an unequal strength, counter-rotating vortex pair has a base state of orbital motion. This imparts an effective rotation to the plane of the sinuous disturbance, shifting the most unstable wavelength. Consequently, the most unstable wavelength for an unequal strength, counter-rotating pair is shorter than that for an equal-strength, counter-rotating pair. The instability is driven by the vortex rate of strain field, which is proportional to the inverse square of the separation distance between the two vortices. Thus, the instability grows significantly faster for a closely spaced flap/tip pair than it does for a widely spaced tip/tip pair. The experimentally observed instability wavelengths agree favorably with those predicted by linear stability analyses for both single and multiple vortex pairs. Computational fluid dynamics simulations in Bristol et al.¹⁹ also highlight several nonlinear features of the instability that were not accessible in the experiments. Having provided the explanations for why this rapidly growing instability occurs, one final point that remains to be discussed is how effective this instability is at alleviating the wake vortex hazard; given the rate at which the instability develops, the rapid spreading of vorticity, and the three-dimensional nature of the resulting wake, the instability in the wake of the triangular-flapped wing is promising to be an effective wake alleviation concept. This paper addresses this question through an analysis of the wake alleviation properties of these triangular-flapped wings.

II. Experimental Setup and Data Processing

PIV measurements are done in a towing tank, which measures 70×2.4 m and has a nominal water depth of 1.5 m. In the middle of the tank is the test section, which has glass windows that give an underwater view of the tank. A lightweight, aluminum carriage is used to tow the wings down the length of the tank at high speeds. The carriage is driven by a 5-hp computer-controlled motor through a steel cable. To minimize the carriage vibration, the proportional, integral, derivative input parameters for the motor are fine tuned. The optimized velocity profile is one in which the carriage undergoes two to three minor oscillations during the initial acceleration before it arrives at a constant velocity 10 m upstream of the test section. Having done flow-visualization experiments from the start of the carriage motion and to the end of the tank, we did not see any influence of these initial transients on the vortex wake behavior being measured. During the experiments, the carriage begins its motion 25 m upstream of the test section and continues until it reaches the far end. The reason for towing the carriage to the end of the tank is that previous experiments have demonstrated that stopping the carriage causes the wake vortices to burst prematurely. This bursting phenomena slowly propagates downstream along the vortices. Therefore, if the carriage is stopped too close to the test section the data collected there soon become contaminated by this effect.

The wings are attached to the carriage by a streamlined strut, which places them approximately 0.5 m beneath the water surface. Before conducting the experiments, flow visualization of the strut

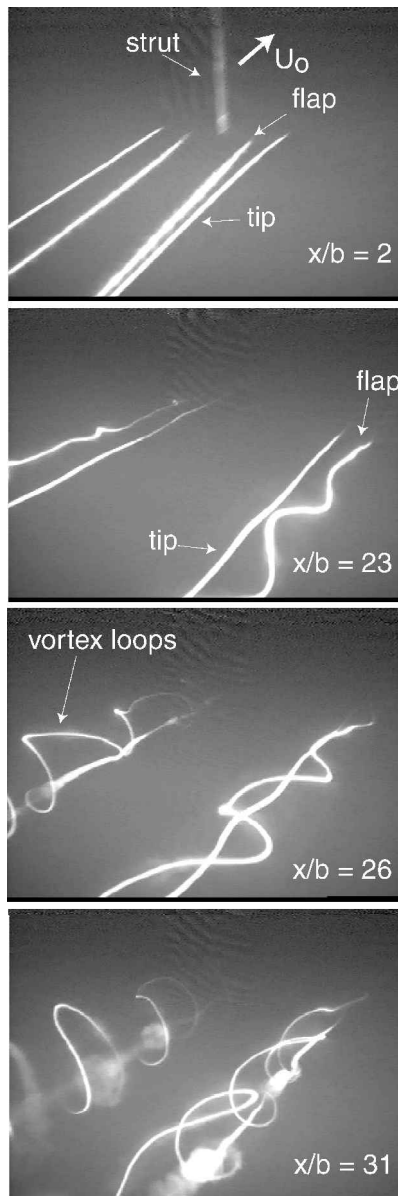


Fig. 1 Dye flow visualization of the instability between unequal strength, counter-rotating flap and tip vortices in the wake of a triangular-flapped wing.¹⁷

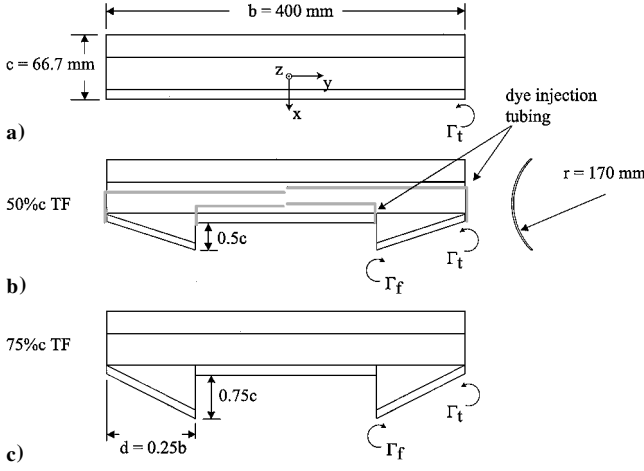


Fig. 2 Planform and side view of the three wings used in the experiment. The dye injection tubing was used in the flow-visualization study in Ortega et al.¹⁸ The right-handed coordinate system (x, y, z) is defined in panel a.

wake is done using particle streaks in a continuous wave laser light sheet to confirm that the strut is not yawed, an effect that could invalidate the subsequent measurements. Slight adjustments are made to the strut's yaw angle so that its wake is as thin as possible. To adjust the wing's angle of attack, the strut can pivot on its mounting bracket, allowing the angle of attack to vary between ± 12 deg in 1-deg increments.

A modular wing (Fig. 2) is used in this experiment to generate the wake vortices. Depending on the type of lift distribution desired, different tabs and flaps can be attached to the trailing-edge of the basic wing. The wing and the trailing-edge tabs and flaps are made of 3.2-mm-thick, stainless-steel sheet metal that is rolled to give a camber radius of 17 cm. The leading edge of the wing is tapered for the first 20 mm, and the trailing-edge tabs and flaps are tapered over the last 10 mm. On the underside of the wing are four 1.1-mm wide \times 1.1-mm deep channels, which house dye injection tubing. For this experiment three wing configurations are used: the basic rectangular-shaped wing, which has a span of $b = 40.0$ cm and a chord of $c = 6.67$ cm; a wing that has a pair of outboard triangular flaps, which have a span of $0.25b$ and a chord of $0.5c$ (denoted hereafter as 50%*c* TF); and a wing that has another pair of outboard triangular flaps, which have a span of $0.25b$ and a chord of $0.75c$ (denoted hereafter as 75%*c* TF). The equi-strength, counter-rotating vortex pair from the rectangular wing serves as a baseline case, against which the wakes of the triangular-flapped wings are compared. A right-handed coordinate system (x, y, z) , which is attached to the wing, is defined in Fig. 2a.

The PIV processing is performed on successive image pairs with an adaptive Lagrangian Parcel Tracking (aLPT) algorithm.^{22,23} This algorithm utilizes interrogation windows that are advected and deformed according to the local velocity and velocity gradient fields, improving the quality of the data in regions of strong deformation. The outputs of aLPT are the two-dimensional velocity vector field u_i and its gradient tensor $\partial u_i / \partial x_j$, which is computed spectrally. For this experiment, processing of the PIV images results in data fields that are 66 bin \times 62 bin, giving a resolution of 1 cm/bin with a 50% overlap between adjacent bins.

Several tests are performed on aLPT to determine its accuracy in measuring the velocity and velocity gradient fields. These tests are accomplished by constructing synthetic PIV images in which the particles are advected according to a known velocity distribution. The images are rendered in IDL (Interactive Data Language) by generating a random distribution of particles over a 1008×1018 data array, which is the same size as the PIV camera's charge-coupled device. Each particle has a Gaussian intensity distribution, where the width of the Gaussian is one pixel and the peak value is a random number between 0 and 255. The particle density is chosen so that the images appear comparable to those of the experimental data. Using a second-order Adams-Bashforth scheme, the particles are then advected by the velocity field of a Lamb-Oseen vortex. The

Table 1 Parameters for the three experimental runs discussed here

Run	Wing	U_0 , cm/s	α , deg	Re_c	Re_Γ	$\bar{\Gamma}_{0f} / \bar{\Gamma}_{0r}$
13	Rect.	500	3	330,000	82,000	—
38	50% <i>c</i> TF	500	2	330,000	101,000	−0.37
47	50% <i>c</i> TF	500	−1	330,000	55,000	−0.56

circulation strength Γ_0 and core size σ of the Lamb-Oseen vortex are chosen to roughly match those of the experimental data. These values are used to generate the synthetic PIV data, which are processed with aLPT. From these tests it is determined that the standard deviation between the analytical and measured vorticity and velocity fields are approximately 3.1 and 4.2% of the maximum analytical vorticity and velocity values, respectively. These values are taken as estimates of the experimental accuracy. However, the actual data contain some out-of-plane motion, meaning that the axial velocity in the vortex wake carries particles through the light sheet. This loss of particles might introduce an additional experimental uncertainty, which has not been accounted for in the preceding analyses.

With the two-dimensional velocity and velocity gradient fields obtained from aLPT, flow statistics for a given run are calculated for the entire field of view, as well as for the individual vortices. Ortega et al.¹⁸ describe several quantities that are calculated. However, only those relevant to the present wake alleviation study are discussed next. The analysis of the vortex wake begins with the first frame in which the wing enters the field of view and continues until the last frame in the run or until the vortices leave the camera's field of view, whichever comes first. The wake's circulation Γ_{tot} is obtained by integrating the axial vorticity ω :

$$\Gamma_{tot} = \int \omega dA \quad (1)$$

and the position $y_c = (y_c, z_c)$ of the overall vorticity centroid from

$$y_c = \frac{1}{\Gamma_{tot}} \int y \omega dA \quad (2)$$

The radial vortex structure $\Gamma(r)$ is obtained by fitting the circulation distribution of a Lamb-Oseen vortex:

$$\Gamma(r) = \Gamma_0 (1 - e^{-r^2/\sigma^2}) \quad (3)$$

to the circulation data of the vortices, where Γ_0 is the vortex strength, σ a measure of the vortex size, and r the distance from vortex centroid.

For the triangular-flapped wings, analysis of the flap and tip vortices continues until the instability gives rise to strong three-dimensional effects in the measurement plane. This criterion is somewhat subjective because it depends on where the PIV light sheet cuts the vortex wake. Typically, the flap and tip vortices are examined until there is a rapid change in their core sizes or until they begin to merge with each other. After this time calculations for the individual vortices cease, and the analysis continues only for those values computed over the entire field of view. For the rectangular wing the tip vortices are examined over the entire run.

A total of 11 runs with the rectangular wing and 24 runs with the triangular-flapped wings are done by varying the towing speed U_0 between 300 and 500 cm/s and the angle of attack α between -1 and 3 deg.¹⁸ The corresponding chord-based Reynolds numbers $Re_c = cU_0/\nu$ are 2.0×10^5 and 3.3×10^5 . The circulation-based Reynolds numbers $Re_\Gamma = \Gamma_{tot}/\nu$ depend on the lift on the wings and range 3.8×10^4 – 1.1×10^5 ; $\nu = 0.01$ cm²/s is used for the kinematic viscosity of water. Table 1 shows the parameters for the three experimental runs discussed in detail in this paper. For the rectangular wings both the port and starboard side vortices are captured in the PIV images (Fig. 3a). However, because the wakes of the triangular-flapped wings spread out so much only the starboard half of triangular-flapped wings is imaged (Fig. 3b).

III. Rolling Moment and Downwash Estimates

Previous investigations of wake alleviation concepts have measured the forces on following aircraft to determine how effective a particular concept was at reducing the wake hazard.^{1,3,4,24–28} For

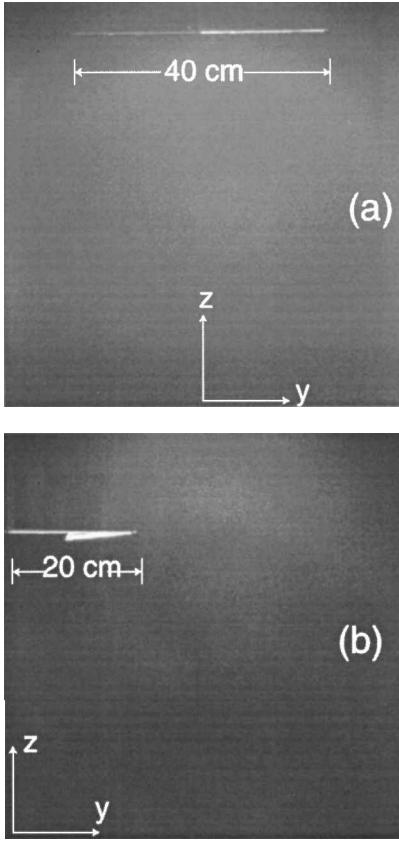


Fig. 3 Reference image of a) the rectangular wing and b) the 50% c TF wing in the view of the PIV camera.

flight tests this often involved flying a smaller airplane into the wake of a larger commercial transport. In more controlled experiments various model planes and wings were positioned or towed in the wake of a larger model airplane. In the present experiment it was not feasible to set up a similar type of test for the triangular-flapped wings. However, what is available are the two-dimensional velocity fields from the moment of formation of the vortex wake up to several hundred spans downstream. With this information it is possible to estimate the forces that a simulated, following wing might experience as it travels in the vortex wakes. Rossow⁵ performed a similar analysis using an analytical velocity distribution. In the calculations to follow, an approach similar to that of Rossow⁵ is followed using the measured velocity fields.

A. Formulation

A schematic of the flowfield is shown in Fig. 4. The simulated following wing is located at (y, z) and has a span of b_f . The (y', z') coordinate system is fixed with respect to the following wing and has its origin at the wing's center (Fig. 5). The flow inclination angle is α_f , and the flow speed about the wing is $V = \sqrt{(U^2 + w^2)}$, where U is the translational velocity of the wing and w is the vertical component of the measured velocity field. The force on a differential portion of the following wing is given by $dL_z = \frac{1}{2} C_{l\alpha_f} \alpha_f \rho V^2 c_f \cos \alpha_f dy'$, where $C_{l\alpha_f}$ is the two-dimensional lift-curve slope, ρ is the fluid density, and c_f is the chord of the following wing. It is assumed that the following wing travels at the same velocity as the towed wings, such that $U = U_0$. From the velocity field measurements the maximum value of $|w/U_0|$ is about 0.15, which implies that $w/U_0 = \tan \alpha_f \approx \alpha_f$, $V \approx U_0$, and $\cos \alpha_f \approx 1$. The total force L_z , defined as the downwash, is obtained by integrating dL_z over the span of the following wing to give

$$L_z = \int_{-b_f/2}^{b_f/2} \frac{1}{2} C_{l\alpha_f} \alpha_f \rho U_0^2 c_f dy' = \frac{1}{2} C_{l\alpha_f} \rho U_0^2 c_f \int_{-b_f/2}^{b_f/2} \frac{w(y', z')}{U_0} dy' \quad (4)$$

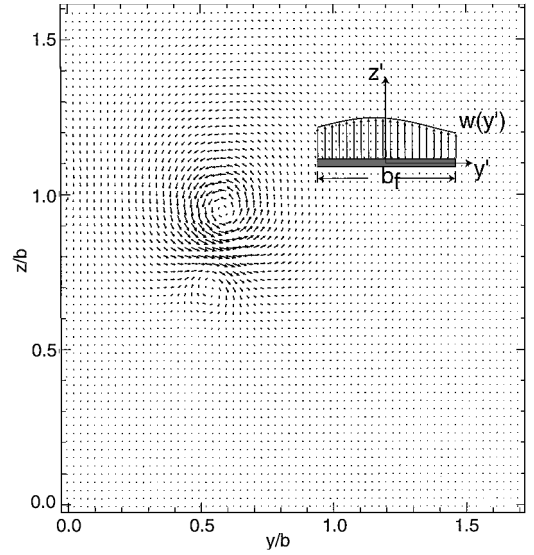


Fig. 4 Schematic of the following wing, which has a span of b_f , in a typical velocity field.

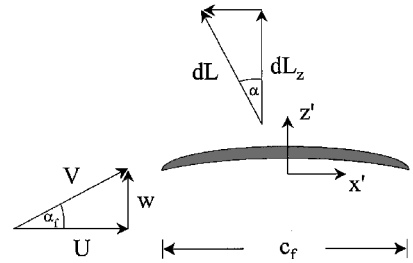
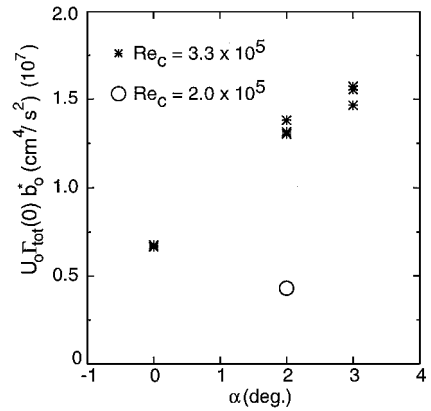
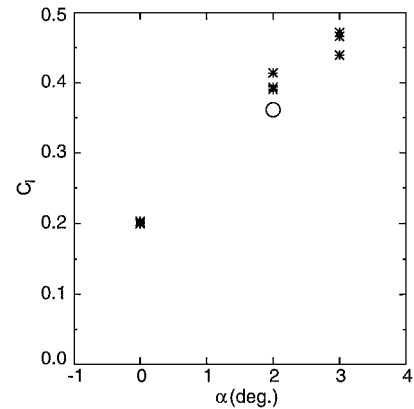


Fig. 5 Cross section of the flow about the following wing in Fig. 4.



a) Lift, $U_0 \Gamma_{\text{tot}}(0) b_0^*$



b) Lift coefficient C_l

Fig. 6 Lift characteristics of the rectangular wing.

where it has been assumed that c_f is constant. Dividing Eq. (4) by b_f gives the average vertical force on the following wing at the location (y, z) . For the sake of simplicity, only the integral quantity

$$D = \frac{1}{b_f} \int_{-b_f/2}^{b_f/2} w(y', z') dy' \quad (5)$$

is used as the downwash in the present analysis. The average rolling moment M_z on the following wing is computed in a similar manner, by evaluating

$$\begin{aligned} M_z &= \frac{1}{b_f} \int_{-b_f/2}^{b_f/2} \frac{1}{2} C_{l\alpha_f} \alpha_f \rho U_0^2 c_f y' dy' \\ &= \frac{1}{2} C_{l\alpha_f} \rho U_0^2 c_f \frac{1}{b_f} \int_{-b_f/2}^{b_f/2} y' \frac{w(y', z')}{U_0} dy' \end{aligned} \quad (6)$$

Again, only the quantity

$$R = \frac{1}{b_f} \int_{-b_f/2}^{b_f/2} y' w(y', z') dy' \quad (7)$$

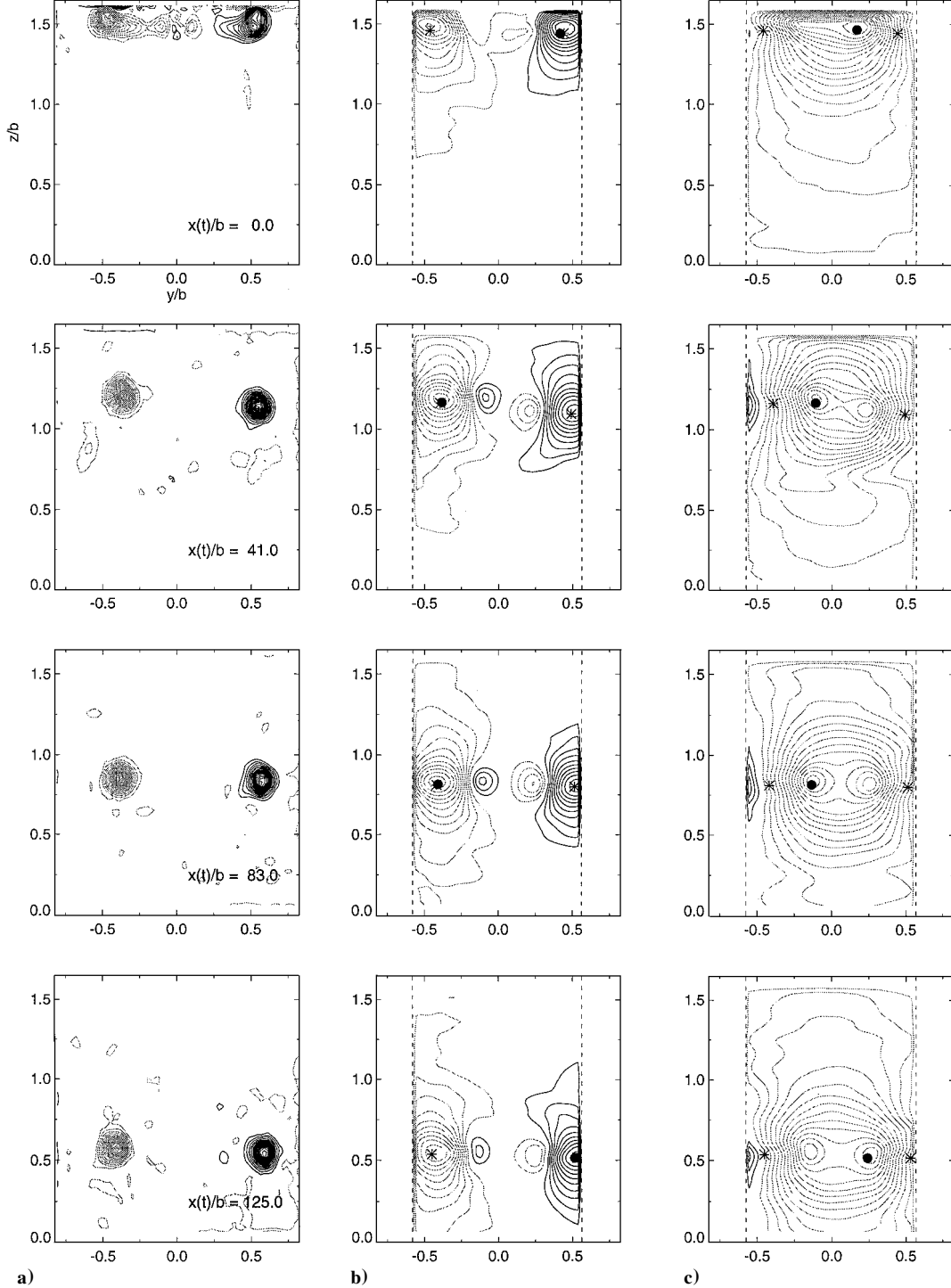


Fig. 7 Contours of a) axial vorticity, b) rolling moment, and c) downwash in the wake of the rectangular wing (run 13, $U_0 = 500$ cm/s, and $\alpha = 3.0$ deg). The symbols * denote the location of the left and right vorticity centroids. The symbols • denote the location of the maximum rolling moment $R_{\max}(t) = \max[R(x(t), y, z)]$, and minimum downwash $D_{\min}(t) = \min\{D[x(t), y, z]\}$. Because the wake is nearly symmetric, the locations of the maximum rolling moment and minimum downwash switch occasionally from one side of the wake to the other.

is considered in the discussion to follow. Because the vortex wake hazard is particularly dangerous for smaller aircraft, the span of the following wing is taken to be $b_f = 20$ cm or half that of the leading wings. By varying the location (y, z) of the following wing, the calculations of Eqs. (5) and (7) are repeated over the entire flowfield, yielding a two-dimensional distribution of the downwash and rolling moment on the following wing. Given the finite span of the following wing, Eqs. (5) and (7) cannot be computed along the left and right sides of the flowfield. Therefore, for the rectangular wing measurements the downwash and rolling moment data are cropped by $b_f/2 = 10$ cm on the left- and right-hand sides of the measurement plane. For the triangular-flapped wings a slightly different method of cropping is done, as discussed in Sec. III.C.

B. Rectangular Wing

We take the wake of the rectangular wing as a baseline case. The lift of the wing is shown in Fig. 6. The quantity $U_0 \Gamma_{\text{tot}}(0) b_0^*$ in Fig. 6a is taken as an estimate of the lift generated by the wing, where $\Gamma_{\text{tot}}(0)$ is the initial circulation in the vortex wake and b_0^* is the lateral distance between the vorticity centroids on either side of the wake at 0 spans. The lift coefficient C_l is shown in Fig. 6b. The

plot indicates that the wing is not stalling over this range of α . The spread in the data points at a given angle of attack and Re_c also gives an indication of the repeatability of the PIV measurements. The lift is finite at $\alpha = 0$ deg, which is expected as a result of the camber on the wing.

Figure 7 shows contours of axial vorticity, rolling moment, and downwash for run 13 ($U_0 = 500$ cm/s, $\alpha = 3.0$ deg). The positive contours are drawn in black and the negative ones in gray. The axial vorticity data are shown to highlight the vortices and to orient the reader to the flow at the various downstream locations. For further discussions of the vorticity data, the reader is referred to Ortega et al.¹⁸ The centroid locations of the left and right vortices are denoted by * and the quantities $D_{\min}(t) = \min\{D[x(t), y, z]\}$ and $R_{\max}(t) = \max\{R[x(t), y, z]\}$ by •. The data fields are cropped along the left and right borders for the reason just discussed. The rolling moment is greatest near the cores of the vortices, whereas the downwash is greatest somewhat inboard of the vortices. Because the wake is nearly symmetric, the locations of the maximum rolling moment $R_{\max}(t)$ and minimum downwash $D_{\min}(t)$ switch occasionally from one side of the wake to the other. Qualitatively, the plots on one side of the wake in Fig. 7 appear similar to those in Rossow⁵

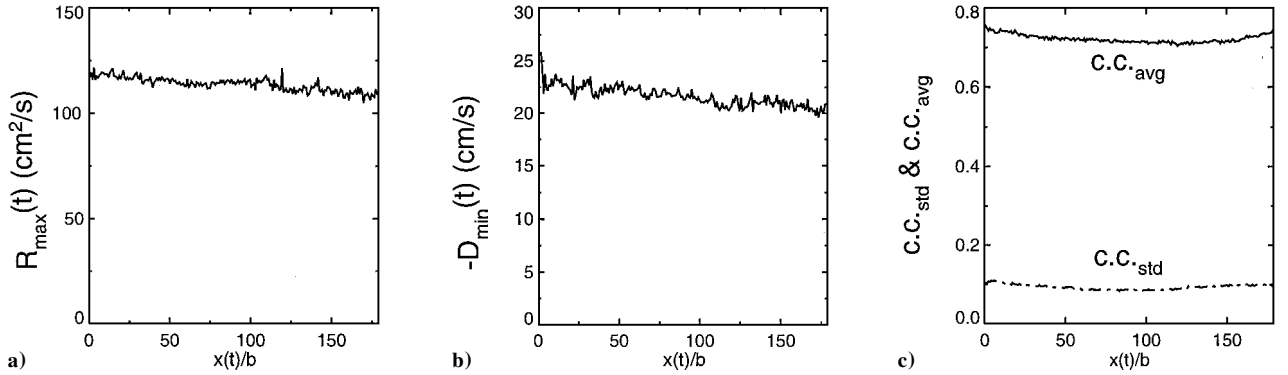


Fig. 8 Functions of downstream distance from the rectangular wing (run 13, $U_0 = 500$ cm/s, and $\alpha = 3.0$ deg): a) maximum rolling moment, b) minimum downwash, and c) average and standard deviation of the correlation coefficient data fields from aLPT.

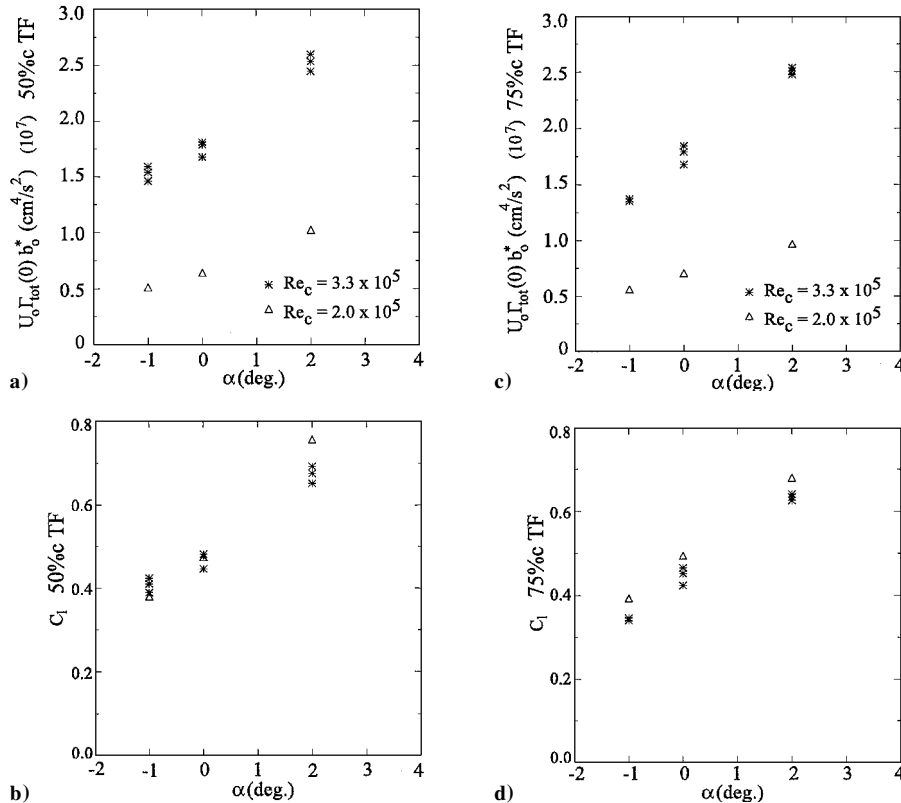


Fig. 9 Lift, $U_0 \Gamma_{\text{tot}}(0) b_0^*$ (a and c) and lift coefficient C_l (b and d) as functions of the angle of attack α for the 50% TF and 75% TF wings.

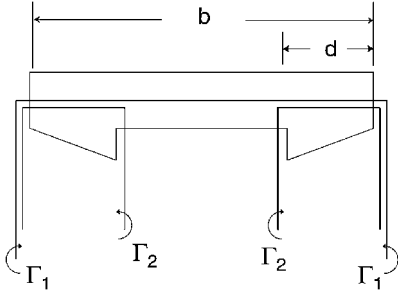


Fig. 10 Simple horseshoe vortex model of the flap and tip vortices generated by the triangular-flapped wings.

for a single vortex. The rolling moment and downwash contours exhibit only slight changes over the course of the run.

The maximum rolling moment $R_{\max}(t)$ and minimum downwash $D_{\min}(t)$ are plotted in Fig. 8 as functions of downstream distance. The downstream distance $x(t)$ is obtained from $U_0 t$, where t is the time since the wing traveled through the vertical PIV light sheet. Because the vortices remain coherent during the entire data run, the downwash and rolling moment exhibit very little decay over the 180 spans of measurements. Consequently, the wake of the rectangular wing is just as “dangerous” to the $b/2$ span wing at 180 spans as it is at 0 span.

Figure 8c shows the average correlation coefficient $c.c._{\text{avg}}$ and the standard deviation of the correlation coefficient $c.c._{\text{std}}$ for each

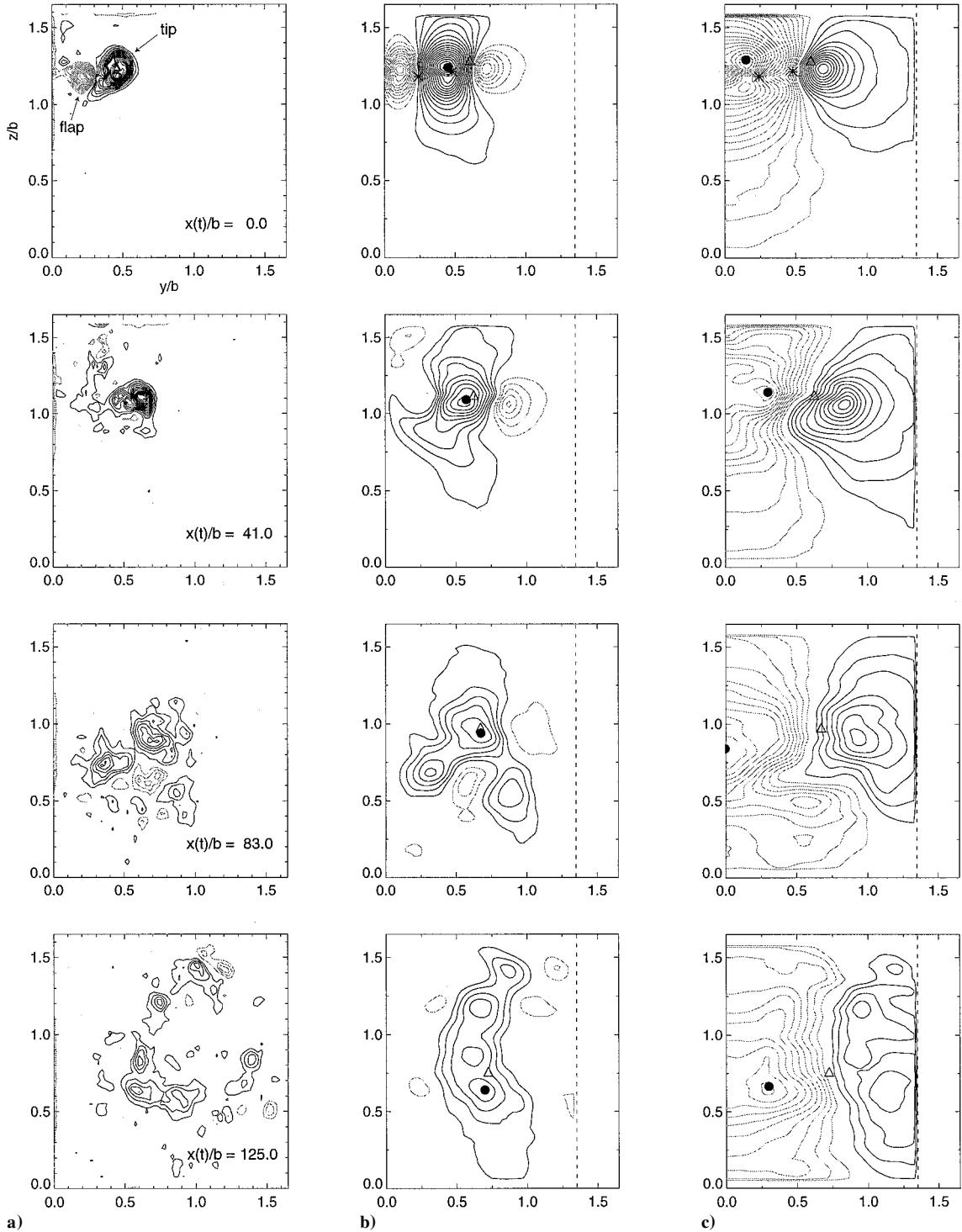


Fig. 11 Contours of a) axial vorticity, b) rolling moment, and c) downwash in the wake of the 50% c TF wing (run 38, $U_0 = 500$ cm/s, and $\alpha = 2.0$ deg). The symbol * denotes the location of the flap and tip vorticity centroids. The symbols • denote the location of the $R_{\max}(t) = \max[R[x(t), y, z]]$ and $D_{\min}(t) = \min[D[x(t), y, z]]$. The symbol Δ shows the location of the starboard-side vorticity centroid.

processed data field from aLPT. This plot can be taken as a “goodness” measure of the PIV data during the run time. For this run the value of $c.c._{avg}$ remains slightly greater than 0.7. Additionally, $c.c._{std}$ is approximately equal to 0.1 over the entire run. For correlation values equal to 1, there is perfect correlation between the sequential particle images. This would occur when there is no fluid motion in the camera’s field of view. The correlation value would be small if the vortex wake is so three-dimensional that all of the particles in the first image leave the light sheet and are replaced with new ones by the time the second image is captured. In the following discussions the plot in Fig. 8c will be used as a reference to determine how good the PIV data are in the wakes of the triangular-flapped wings.

C. Triangular-Flapped Wings

Figure 9 shows $U_0 \Gamma_{tot}(0) b_0^*$ and C_l for the 50% c TF and 75% c TF wings as functions of α . The lift generated by the triangular-flapped wings is considerably greater than that of the rectangular wing (Fig. 6a) at the same angle of attack and speed. This result might seem counterintuitive given the fact that the oppositely signed flap vortices cancel a portion of the circulation in the wake from the tip vortices. However, a simple horseshoe model of the vortex wake shown in Fig. 10 illustrates why the lift is greater for the triangular-flapped wings. In Fig. 10 the vortex wake is modeled by three vortex filaments: two horseshoe vortices of strength Γ_2 from the triangular flaps and a single horseshoe filament of strength Γ_1 from the rectangular portion of the wing. The distance between the legs of the Γ_1 filament is b , whereas that for the Γ_2 filaments is d . Without the flap vortices the distance b^* between the circulation centroids on either side of the wake is b , and the corresponding lift is proportional to $\Gamma_1 b^* = \Gamma_1 b$. Placing the counter-rotating flap vortices next to the tip vortices changes the distance b^* between the circulation centroids. Therefore, the lift is proportional to $(\Gamma_1 + \Gamma_2 - \Gamma_2)b^* = \Gamma_1[b + 2(\Gamma_2/\Gamma_1)d]$, which is greater than the lift generated by the single horseshoe filament of strength Γ_1 .

The PIV measurements for the triangular-flapped wings are only made on the starboard-side of the wake, preventing the rolling moment and downwash from being calculated at the wake centerline. This is caused by the finite span of the following wing, which crops the contours by 10 cm on either side of the measurement plane. Consequently, the quantities $R_{max}(t)$ and $D_{min}(t)$ might be in error, especially if they have extrema near the wake centerline. To remedy this potential source of error, a mirror image of the velocity field is placed on the left side of the original velocity field, in effect, generating a port-side, counter-rotating vortex pair. With this four-vortex wake $R_{max}(t)$ and $D_{min}(t)$ can be computed at the wake centerline. This reflection technique is not quite exact because the wakes of the triangular-flapped wings are not exactly symmetric. As seen in the flow-visualization pictures,¹⁸ the instability between the flap and tip vortices develops independently on either side of the wake. Additionally, what is called the centerline of the triangular-flapped wings might have a slight error. Because the interrogation windows in aLPT are not integer multiples of the image size, the PIV image is cropped along its borders. This subsequently introduces an uncertainty of about 2cm in the centerline location. Therefore, the reader should keep in mind these shortcomings in the following discussions.

Figure 11 shows in columns contours of axial vorticity, rolling moment, and downwash, respectively, for the 50% c TF wing at $U_0 = 500$ cm/s and $\alpha = 2$ deg (run 38). The flap-to-tip vortex strength ratio $\bar{\Gamma}_{of}/\bar{\Gamma}_{ot}$ is -0.37 , where $\bar{\Gamma}_{of}$ and $\bar{\Gamma}_{ot}$ are the average circulations of the flap and tip vortices. For each column of plots, the same contour levels are used. The vorticity data are shown to orient the reader to the flow at the various downstream locations. At $x(t)/b = 0$ the rolling-moment contours vary from negative to positive to negative as one proceeds outboard from the wake centerline. The symbol \bullet in these plots indicates the location of the maximum rolling moment $R_{max}(t)$ and the symbol $*$ the locations of the flap and tip vortices. The symbol Δ marks the location of the overall vorticity centroid. As the instability between the flap and tip vortices becomes nonlinear, the distribution of the rolling moment becomes more widespread. By 125 spans the rolling-moment contours cover

a large region of the measurement plane, and the maximum rolling moment has dropped significantly from its value at $x(t)/b = 0$.

Contours of downwash on the following wing are shown in the third column of Fig. 11. Unlike the rolling moment, the minimum downwash $D_{min}(t)$ (\bullet) occurs inboard of the flap and tip vortices. In fact, the location of minimum downwash at $x(t)/b = 0$ occurs at $y/b \leq 0.25$, indicating that this value would not have been computed if the velocity field reflection were not performed. One interesting observation from Fig. 11 is the lateral spreading of the downwash. At $x(t)/b = 0$ the negative contours are located at $y/b < 0.5$. However, by 125 spans the instability has spread these negative contours, such that they are now located at $y/b < 0.75$.

Fig. 12a Maximum rolling moment $R_{max}(t)$.

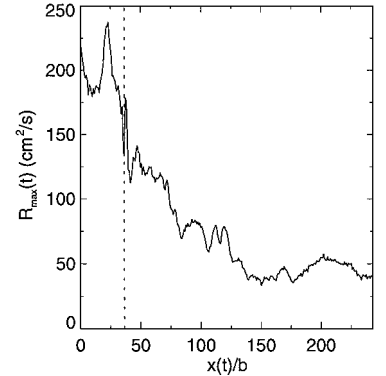


Fig. 12b Minimum downwash $D_{min}(t)$ for run 38 ($U_0 = 500$ cm/s, $\alpha = 2.0$ deg, 50% c TF, $\bar{\Gamma}_{of}/\bar{\Gamma}_{ot} = -0.37$).

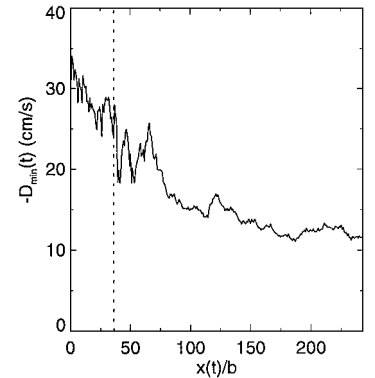


Fig. 12c Flap, tip, and overall vorticity centroids. (Increasing time is indicated by the arrows.)

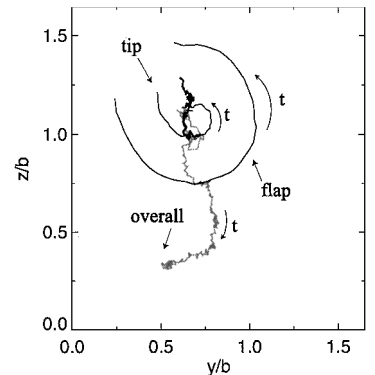
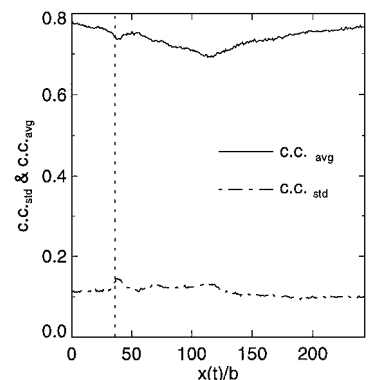


Fig. 12d Average and standard deviation of the correlation coefficient data fields from aLPT for run 38.



Figures 12a and 12b shows the trends of maximum rolling moment $R_{\max}(t)$ and minimum downwash $D_{\min}(t)$ over the course of run 38. The trajectories of the flap and tip vortices, as well as that of the overall centroid, are shown in Fig. 12c to demonstrate the position of the wake during the measurement period. The curved black lines are the positions of the flap and tip vortices prior to the rapid change in vortex structure at 36 spans. The thick, black line denotes the centroid of the wake for $x(t)/b < 36$, whereas the gray line marks it for $x(t)/b \geq 36$. Prior to 36 spans (vertical dashed line), the rolling moment undergoes oscillations in which it has local maxima at $x(t)/b = 0$ and $x(t)/b \approx 25$ and a local minimum at $x(t)/b \approx 10$. The reason for this fluctuation is the change in the orientation of the

counter-rotating pair. At $x(t)/b = 0$ and $x(t)/b \approx 25$ the flap and tip vortices are horizontally aligned and, therefore, impart a larger rolling moment on the following wing. At $x(t)/b \approx 10$ the vortices are vertically aligned, and the corresponding rolling moment is less. At 36 spans the vortex cores undergo a sudden change in structure, as the instability becomes nonlinear. After this location the rolling moment decreases substantially and continues to decay over the rest of the run. By 243 spans the rolling moment has decreased by approximately 80% from its initial value. The downwash for run 38 is shown in Fig. 12b. Like the trends of the rolling moment, the downwash decays considerably over the run as the wake becomes increasingly three-dimensional and incoherent. The average and standard

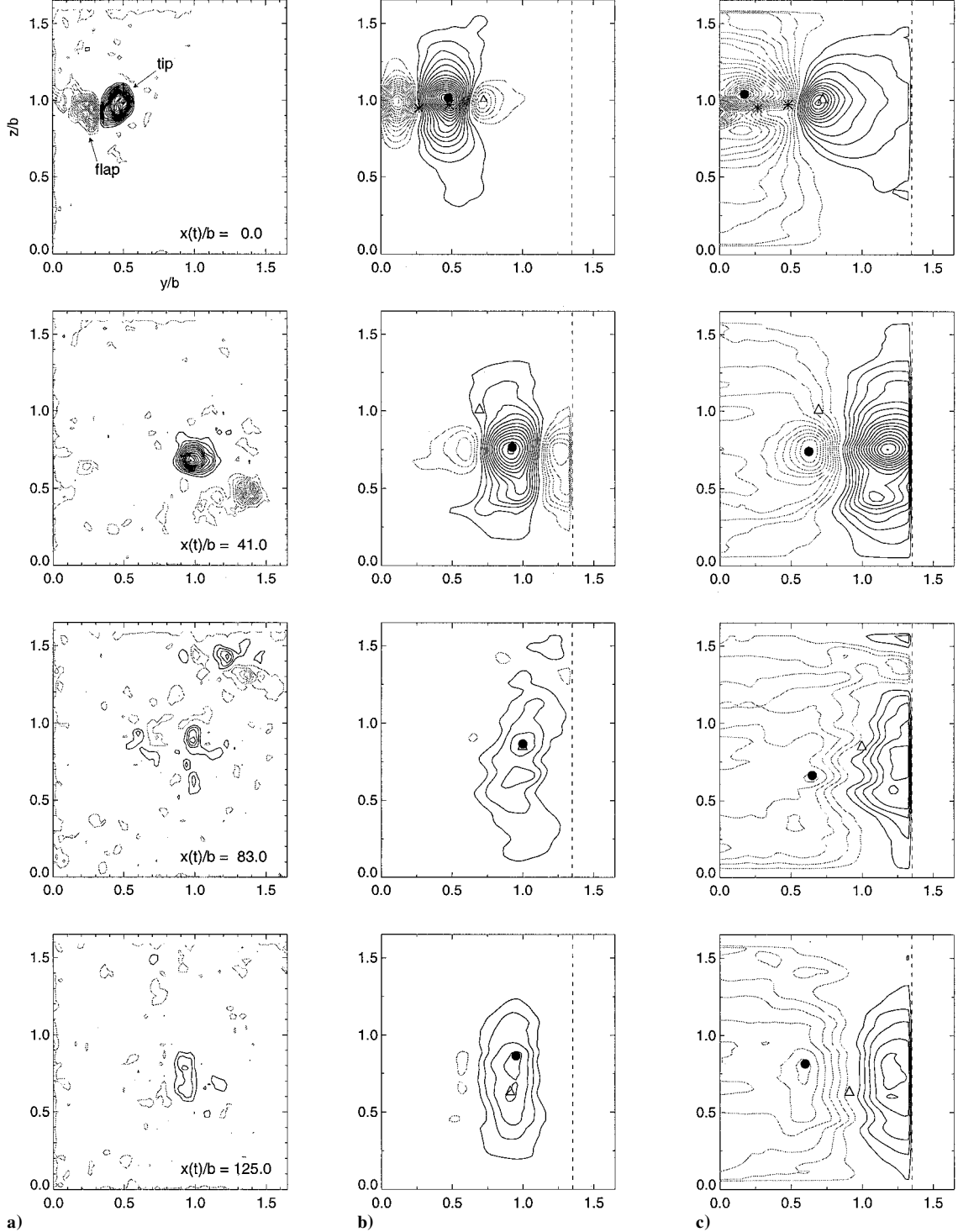


Fig. 13 Contours of a) axial vorticity, b) rolling moment, and c) downwash in the wake of the 50% TF wing (run 47, $U_0 = 500$ cm/s, and $\alpha = -1.0$ deg). The symbol * denotes the location of the flap and tip vorticity centroids. The symbols • denote the location of the $R_{\max}(t) = \max[R(x(t), y, z)]$ and $D_{\min}(t) = \min[D(x(t), y, z)]$. The symbol Δ shows the location of the starboard-side vorticity centroid.

deviation of the correlation coefficient from aLPT is shown in Fig. 12d. Although $c.c._{avg}$ decreases somewhat over the course of the run, it remains at values comparable to those of the rectangular wing's wake (Fig. 8). Likewise, $c.c._{std}$ has values that are about equal to those of the rectangular wing in run 13. This demonstrates that the time (6 ms) between the sequential PIV images is small enough to reduce the amount of particles leaving the light sheet. If the maximum axial velocity of the particles is taken to be on the order of the maximum azimuthal velocity in the vortices (≈ 50 cm/s; see Fig. 31 in Ref. 18), the particles move about 0.25 cm axially, which is less than the thickness (1 cm) of the light sheet. Consequently, aLPT can measure the two-dimensional velocity and velocity gradient fields despite the fact that the wake becomes highly three-dimensional.

For larger values of $|\bar{\Gamma}_{0f}/\bar{\Gamma}_{0t}|$, the qualitative features of the downwash and rolling-moment distributions are similar to those just described. Figure 13 shows this for run 47 ($U_0 = 500$ cm/s, $\alpha = -1.0$ deg, 50% c TF, $\bar{\Gamma}_{0f}/\bar{\Gamma}_{0t} = -0.56$). Once again the negative contours of downwash exhibit lateral spreading and the rolling-moment distribution grows more diffuse as a result of the wake instability. Figures 14a and 14b show the time-varying values of $R_{max}(t)$ and $D_{min}(t)$. At 40 spans the structure of the vortex cores suddenly changes, and the rolling moment and downwash decrease. Over the rest of the run, both the downwash and rolling moment demonstrate little decay. Because $|\bar{\Gamma}_{0f}/\bar{\Gamma}_{0t}|$ is larger in this run than that in run 38, the flap and tip vortices trace out paths that have larger radii of curvature (Fig. 14c). Additionally, $c.c._{avg}$ and $c.c._{std}$ have values that are near those of the rectangular wing over the entirety of the run.

From the data in runs 13, 38, and 47, it can be seen that the downwash and rolling moment of the triangular-flapped wings behave in a manner quite unlike that of the rectangular wing. However, because the wings in these runs generate unequal amounts of lift a more accurate comparison must be made by nondimensionalizing by the lift of the wings, which is proportional to $U_0 \Gamma_{tot}(0) b_0^*$. To make a proper comparison, the lift of the rectangular and triangular-flapped wings is equated to the lift generated by a simple horseshoe vortex of strength Γ_h , where

$$\Gamma_h = (b_0^*/b) \Gamma_{tot} \quad (8)$$

For the rectangular wing in run 13, $\Gamma_h = 740$ cm²/s. On the other hand, $\Gamma_h = 1220$ cm²/s for run 38 and $\Gamma_h = 800$ cm²/s for run 47.

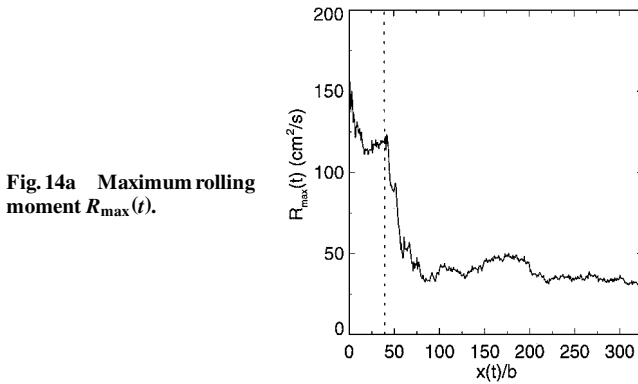


Fig. 14a Maximum rolling moment $R_{max}(t)$.

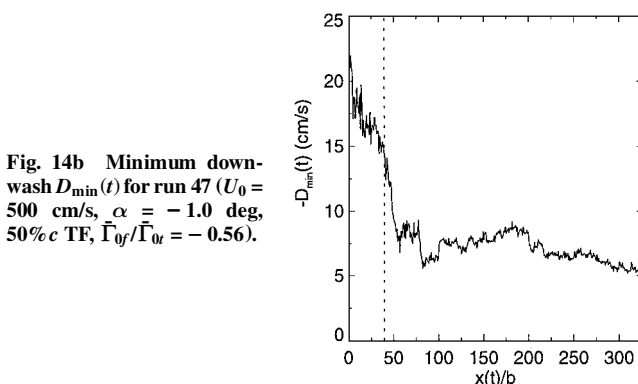


Fig. 14b Minimum downwash $D_{min}(t)$ for run 47 ($U_0 = 500$ cm/s, $\alpha = -1.0$ deg, 50% c TF, $\bar{\Gamma}_{0f}/\bar{\Gamma}_{0t} = -0.56$).

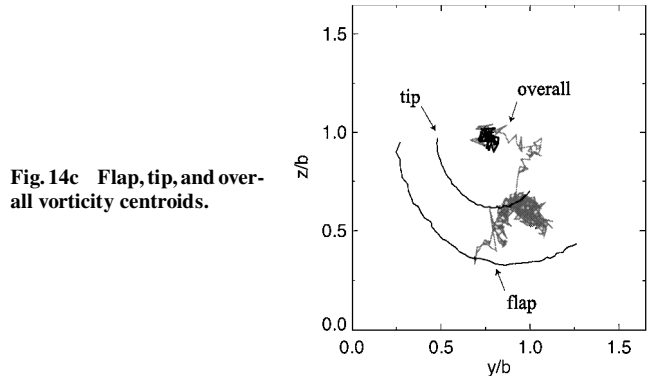


Fig. 14c Flap, tip, and overall vorticity centroids.

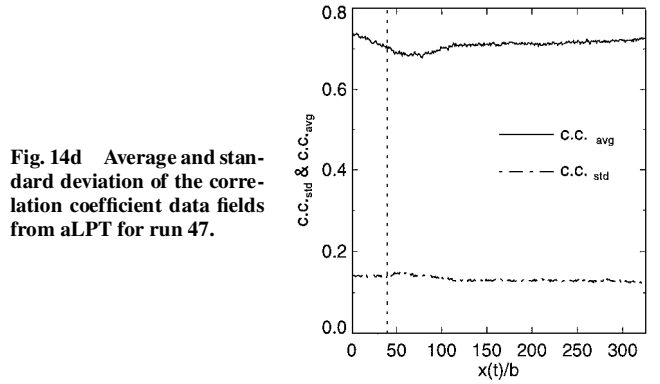
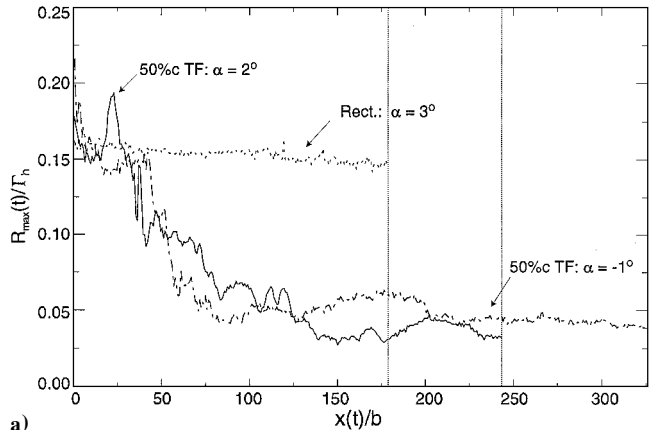
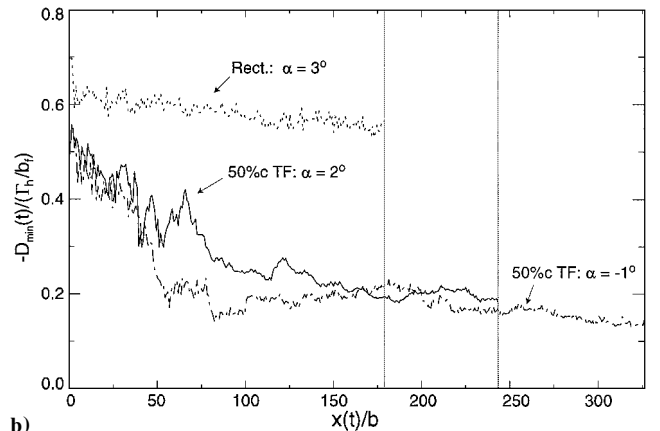


Fig. 14d Average and standard deviation of the correlation coefficient data fields from aLPT for run 47.



a)



b)

Fig. 15 Dimensionless a) maximum rolling moment $R_{max}(t)/\Gamma_h$ and b) minimum downwash $D_{min}(t)/(\Gamma_h/b_f)$, as functions of downstream location for the rectangular wing (run 13) and the 50% c TF wing at 2.0 deg (run 38) and -1.0 deg (run 47).

Figure 15 shows the dimensionless rolling moment $R_{\max}(t)/\Gamma_h$ and downwash $D_{\min}(t)/(\Gamma_h/b_f)$ for these three runs. Initially, the rolling moments of the 50%*c* TF wing are greater than that of the rectangular wing. As soon as the instability becomes evident in the measurement plane, the rolling moments of the triangular-flapped wing rapidly drop below the value for the rectangular wing. Because the wakes in runs 13 and 38 descend out of view during the measurement period, their rolling moments are only plotted up to 180 and 243 spans. The downwash of the triangular-flapped wing is less than that of the rectangular wing at $x(t)/b = 0$. When the nonlinear effects of the instability propagate through the measurement plane, the downwash begins to decrease. By 150 spans the downwash of the triangular-flapped wing is about $\frac{1}{3}$ of the value for the rectangular wing.

Figure 16 compares $R_{\max}(t)/\Gamma_h$ and $D_{\min}(t)/(\Gamma_h/b_f)$ for the 50%*c* TF, 75%*c* TF, and rectangular wings at three downstream locations [$x(t)/b = 0, 75$, and 150] for all of the runs in Ortega et al.¹⁸ at $U_0 = 500$ cm/s. Again, the rolling moment and downwash have been nondimensionalized to account for the different values of lift in each of these runs. Figures 16a and 16d show that the rolling moment and downwash of the rectangular wing typically

exhibit little decay during the measurement period. The results for the triangular-flapped wings are plotted in Figs. 16b, 16c, 16e, and 16f. The horizontal dashed lines in these figures represent the average values of $R_{\max}(t)/\Gamma_h$ and $D_{\min}(t)/(\Gamma_h/b_f)$ for the rectangular wing at $x(t)/b = 75$. Although the flap extensions of the 75%*c* TF wing are larger than those of the 50%*c* TF wing, the trends in the data are similar. There is not a strong dependence on the flap-to-tip circulation strength ratio $\bar{\Gamma}_{0f}/\bar{\Gamma}_{0t}$. It is evident that the rolling moment and downwash of the triangular-flapped wings decrease noticeably during the first 150 spans. Furthermore, by 75 spans the rolling moment and downwash of the triangular-flapped wings are always less than those of the rectangular wing. For the 50%*c* TF wing the greatest reduction in the rolling moment at $x(t)/b = 75$ occurs for run 44 ($\bar{\Gamma}_{0f}/\bar{\Gamma}_{0t} = -0.49$), in which $R_{\max}(t)/\Gamma_h$ is 62% less than the average value for the rectangular wing at the same downstream location. Also, the 50%*c* TF has the greatest reduction in the downwash in run 47 ($\bar{\Gamma}_{0f}/\bar{\Gamma}_{0t} = -0.56$), in which $D_{\min}(t)/(\Gamma_h/b_f)$ is 65% less than the average value for the rectangular wing at $x(t)/b = 75$. For the 75%*c* TF wing at $x(t)/b = 75$, the reductions at $x(t)/b = 75$ are comparable: a 67% reduction in the rolling moment for run 53

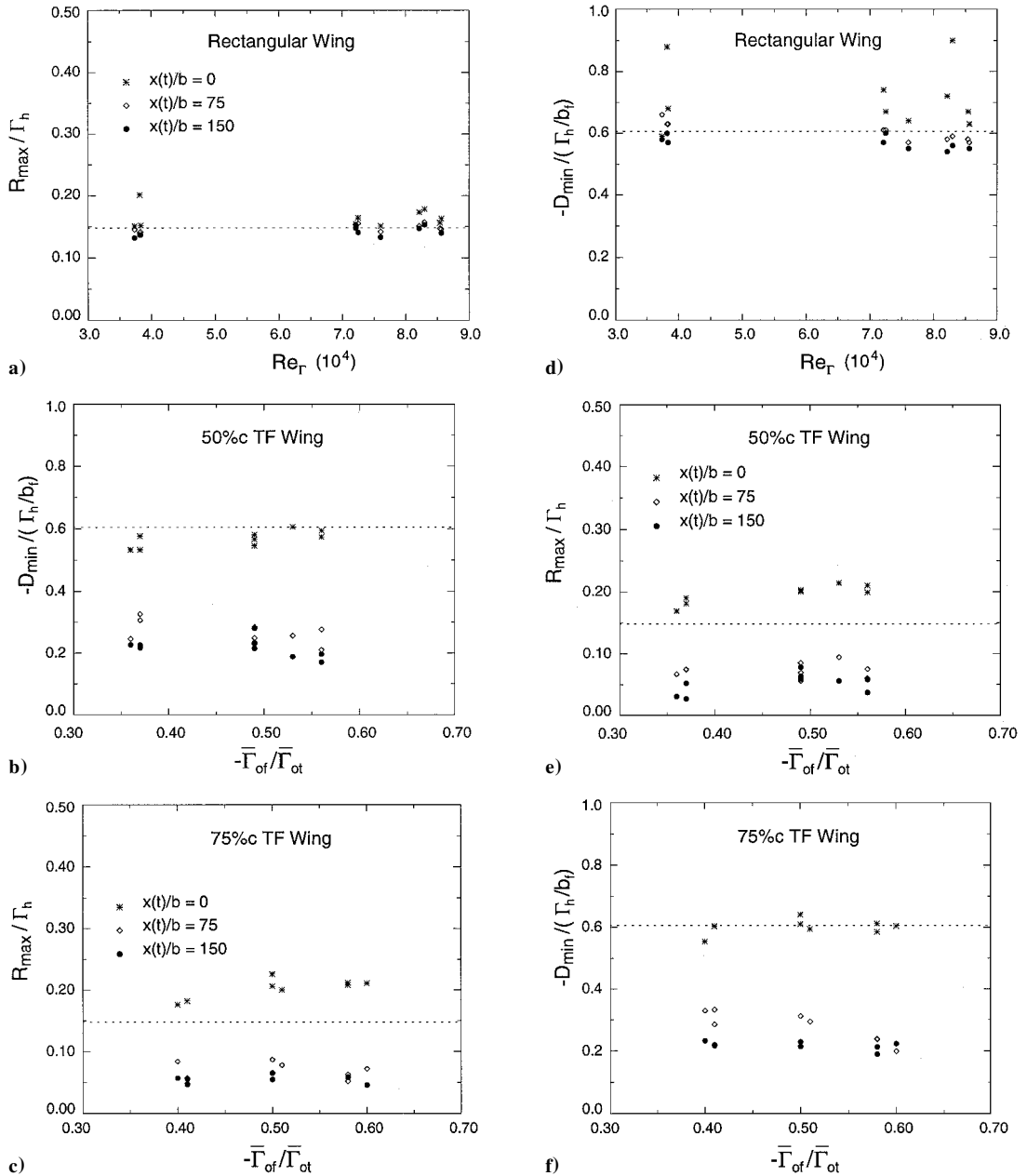


Fig. 16 Dimensionless maximum rolling moment and downwash for the rectangular (a and d), 50%*c* TF (b and e), and 75%*c* TF (c and f) wings at $x(t)/b = 0, 75$, and 150; ---, average values for the rectangular wing at $x(t)/b = 75$.

($\bar{\Gamma}_{0f}/\bar{\Gamma}_{0r} = -0.41$) and a 67% reduction in the downwash for run 59 ($\bar{\Gamma}_{0f}/\bar{\Gamma}_{0r} = -0.60$).

From the data in Fig. 16, an important conclusion is drawn: the 50 and 75% c triangular-flapped wings generate a wake that has a rolling moment and downwash that is significantly less than that of the rectangular wing by 75 spans.

IV. Design Issues

As with many of the proposed concepts for reducing the wake hazard, the triangular-flapped wing design comes with its own set of challenges. The first is that of drag. By generating oppositely signed control vortices, the induced drag on the wing will more than likely increase. However, the triangular flaps would be extended only during takeoff and landing, when following aircraft are relatively close. During landing, the additional drag would not be a problem because the plane is already decelerating. But during takeoff, the added drag would call for higher engine thrust.

The second challenge of this concept is that of structural modifications. In its present form this wake alleviation concept operates by increasing the wing's outboard loading, which generates a larger bending moment in the wing. If this design were incorporated into an airplane, the increased bending moment would have to be compensated by strengthening the wing. For this reason the use of outboard flaps would best be employed on a new aircraft design and not an existing one. Perhaps, a means of circumventing this shortcoming is to use other designs, such as vertically oriented flaps²⁹ or the horizontal stabilizer, to generate oppositely signed control vortices.

Despite the challenges, this wake alleviation concept does possess several advantages. The first is that it is completely passive. Requiring no oscillating flaps or pulsed jets, the triangular-flapped wing design functions by simply placing oppositely signed vortices inboard of the tip vortices and using their presence to disrupt the coherence of the wake. There are no concerns of degraded passenger comfort as there is likely to be in a design that periodically varies the lift distribution or vortex core sizes. Additionally, because the flaps do not oscillate there would be no concerns about maintaining them against structural fatigue.

The second advantage of this concept is that the instability between the flap and tip vortices evolves very rapidly when compared to the Crow instability, the mechanism that typically brings about the demise of the vortex wake. Following Crow's²¹ analytical study of the long-wave instability for a counter-rotating vortex pair, numerous wake alleviation concepts were tested in an effort to hasten this instability.^{2,24,30} The hypothesis was that if this instability could be externally forced to grow the linking of oppositely signed tip vortices would form Crow rings more quickly, hence changing the two-dimensional nature of the wake into a three-dimensional one. The resulting incoherent wake would pose less of a threat to following aircraft. However, one drawback of the Crow instability is its slow growth rate. Typically, it requires a few hundred spans to develop, making it a less attractive candidate for rapid wake attenuation. The primary reason for this slow growth rate is that the large spacing between the tip vortices reduces the rate of strain that they induce on each other. Because the rate-of-strain field is the driving mechanism of the instability's growth, it takes that much longer for the perturbations to become finite in size. On the other hand, by reducing the distance between oppositely signed vortices, as is accomplished with the triangular-flapped wing, the instability can grow more rapidly. Furthermore, once the instability is triggered the nonlinear effects overwhelm the flow. The flow-visualization data in the wakes of the triangular-flapped wings demonstrate that the instability grows to a finite size typically within 15–20 spans downstream of the wing. By 75 spans, at which time the rectangular wing's wake is still descending peacefully, the two-dimensional nature of the triangular-flapped wing's wake has been completely transformed into a three-dimensional one.

The third advantage of this wake alleviation concept is that, although it is passive, its design does allow for the control of the nonlinear evolution of the wake. By varying the relative circulation strength of the flap vortices from only -0.4 to -0.7 , it has been observed that the behavior of the vortex wake can be widely altered.¹⁸ For smaller values of $|\bar{\Gamma}_{0f}/\bar{\Gamma}_{0r}|$, there is a large exchange of vorticity

across the wing centerline in the form of vortex rings. For larger values of $|\bar{\Gamma}_{0f}/\bar{\Gamma}_{0r}|$, the vortices are confined to each side of the wake, and the instability leads to an upward ejection of vorticity. Therefore, depending on the type of behavior desired in the vortex wake and the background flow conditions (wind shear, crosswinds, and turbulence) the strength of the flap vortices can be individually adjusted accordingly.

V. Conclusions

The wake alleviation properties of triangular-flapped wings are estimated by comparing the rolling moment and downwash in the wakes of the triangular-flapped wings with those in the wake of a baseline, rectangular wing. Using planar PIV velocity field data, the rolling moment and downwash are calculated over a simulated following wing, which has a span half that of the wings. For the unmodified, rectangular wing the trailing vortex wake is stable, two-dimensional, and long-lived, resulting in a rolling moment and downwash that exhibit minimal decay over the time of measurements. On the other hand, the triangular-flapped wings generate a trailing vortex wake that has significant wake alleviation properties. The triangular-shaped flaps produce oppositely signed flap vortices near the tip vortices, resulting in a vortex wake comprised of two unequal strength, counter-rotating vortex pairs. Within 15–20 spans these vortex pairs undergo a rapidly growing sinuous instability that transforms the two-dimensional nature of the wake into a three-dimensional one. The resulting distributions of rolling moment and downwash are shown to be highly diffuse when compared to those in the wake of the rectangular wing. Furthermore, both the maximum rolling moment and downwash are approximately one-half the average value for the rectangular wing by 75 spans. This behavior is seen to exist for all of the experimental runs over which the counter-rotating flap vortices have strengths ranging from 40 to 70% of that of the tip vortices. The results demonstrate that the instability in the wake of the triangular-flapped wings offers a possible mechanism for rapid and effective wake alleviation.

Acknowledgment

Robert Bristol and Jason Ortega were recipients of National Science Foundation fellowships.

References

- Dunham, R. E., Jr., "Unsuccessful Concepts for Aircraft Wake Vortex Minimization," *NASA Symposium on Wake Vortex Minimization*, edited by A. Gessow, NASA SP-409, 1976, pp. 221–250.
- Dunham, R. E., Jr., "Exploratory Concepts Found to be Unsuccessful for Aircraft Wake Vortex Minimization," *NASA Symposium on Wake Vortex Minimization*, edited by A. Gessow, NASA SP-409, 1976, pp. 218–257.
- Patterson, J. C., Jr., "Vortex Attenuation Obtained in the Langley Vortex Research Facility," *Journal of Aircraft*, Vol. 12, No. 9, 1975, pp. 745–749.
- Patterson, J. C., Jr., Hastings, E. C., Jr., and Jordan, F. L., Jr., "Ground Development and Flight Correlation of the Vortex Attenuating Spline Device," *NASA Symposium on Wake Vortex Minimization*, edited by A. Gessow, NASA SP-409, 1976, pp. 275–302.
- Rosow, V. J., "Inviscid Modeling of Aircraft Trailing Vortices," *NASA Symposium on Wake Vortex Minimization*, edited by A. Gessow, NASA SP-409, 1976, pp. 4–54.
- Rennich, S. C., and Lele, S. K., "A Method for Accelerating the Destruction of Aircraft Wake Vortices," *Journal of Aircraft*, Vol. 36, No. 2, 1999, pp. 398–404.
- Quackenbush, T. R., Bilanin, A. J., and McKillip, R. M., Jr., "Vortex Wake Control via Smart Structures Technology," *Proceedings of the Society of Photo-Optical Instrumentation Engineers—The International Society for Optical Engineering*, Vol. 2721, Society of Photo-Optical Instrumentation Engineers—The International Society for Optical Engineering, Bellingham, WA, 1996, pp. 78–92.
- Quackenbush, T. R., Bilanin, A. J., Batcho, P. F., McKillip, R. M., Jr., and Carpenter, B. F., "Implementation of Vortex Wake Control Using SMA-Actuated Devices," *Proceedings of the Society of Photo-Optical Instrumentation Engineers—The International Society for Optical Engineering*, Vol. 3044, Society of Photo-Optical Instrumentation Engineers—The International Society for Optical Engineering, Bellingham, WA, 1997, pp. 134–146.
- Quackenbush, T. R., Batcho, P. F., Bilanin, A. J., and Carpenter, B. F., "Design, Fabrication, and Test Planning for an SMA-Actuated Vortex Wake Control System," *Proceedings of the Society of Photo-Optical Instrumentation Engineers—The International Society for Optical Engineering*, Society

of Photo-Optical Instrumentation Engineers—The International Society for Optical Engineering, Bellingham, WA, Vol. 3326, 1998, pp. 259–271.

¹⁰Quackenbush, T. R., Bilanin, A. J., and Carpenter, B. F., “Test Results for an SMA-Actuated Vortex Wake Control System,” *Proceedings of the Society of Photo-Optical Instrumentation Engineers—The International Society for Optical Engineering*, Vol. 3674, Society of Photo-Optical Instrumentation Engineers—The International Society for Optical Engineering, Bellingham, WA, 1999, pp. 84–94.

¹¹Rossow, V. J., “Prospects for Destructive Self-Induced Interactions in a Vortex Pair,” *AIAA Journal*, Vol. 24, No. 7, 1987, pp. 433–440.

¹²Chen, A., Jacob, J., and Savaş, Ö., “Dynamics of Corotating Vortex Pairs in the Wakes of Flapped Airfoils,” *Journal of Fluid Mechanics*, Vol. 383, 1999, pp. 155–193.

¹³Bristol, R., Ortega, J., and Savaş, Ö., “Towing Tank Study of Airfoil Wake Vortices at Re_T of Order 10^5 ,” AIAA Paper 99-3419, June 1999.

¹⁴Donaldson, C., and Bilanin, A., “Vortex Wakes of Conventional Aircraft,” AGARDograph 204, edited by R. H. Korkegi, Aeronautical Research Associates, Princeton, NJ, May 1975.

¹⁵Bilanin, A. J., Donaldson, C. D., and Snedeker, R. S., “An Analytic and Experimental Investigation of the Wakes Behind Flapped and Unflapped Wings,” U.S. Air Force Flight Dynamics Lab., AFFDL-TR-74-90, Aeronautical Research Associates of Princeton, Princeton, NJ, Sept. 1974.

¹⁶Ortega, J. M., and Savaş, Ö., “Rapidly Growing Instability Mode in Trailing Multiple-Vortex Wakes,” *AIAA Journal*, Vol. 39, No. 4, 2001, pp. 750–754.

¹⁷Ortega, J. M., “Stability Characteristics of Counter-Rotating Vortex Pairs in the Wakes of Triangular-Flapped Airfoils,” Ph.D. Dissertation, Dept. of Mechanical Engineering, Univ. of California, Berkeley, CA, Jan. 2001.

¹⁸Ortega, J. M., Bristol, R. L., and Savaş, Ö., “Experimental Study of the Instability of Unequal Strength Counter-Rotating Vortex Pairs,” *Journal of Fluid Mechanics* (submitted for publication).

¹⁹Bristol, R. L., Ortega, J. M., Marcus, P. S., and Savaş, Ö., “Cooperative Instabilities of a Parallel Vortex Pair,” *Journal of Fluid Mechanics* (submitted

for publication).

²⁰Widnall, S. E., Bliss, D. B., and Tsai, C.-Y., “The Instability of Short Waves on a Vortex Ring,” *Journal of Fluid Mechanics*, Vol. 66, No. 1, 1974, pp. 35–47.

²¹Crow, S. C., “Stability Theory for a Pair of Trailing Vortices,” *AIAA Journal*, Vol. 8, No. 12, 1970, pp. 2172–2179.

²²Sholl, M. J., and Savaş, Ö., “A Fast Lagrangian PIV Method for Study of General High-Gradient Flows,” AIAA Paper 97-0493, Jan. 1997.

²³Tsuei, L., and Savaş, Ö., “Treatment of Interfaces in Particle Imaging Velocimetry,” *Experiments in Fluids*, Vol. 29, No. 3, 2000, pp. 203–214.

²⁴Barber, M. R., and Tymczyszyn, J. J., “Wake Vortex Attenuation Tests: A Status Report,” 1980 Aircraft Safety and Operating Problems, NASA CP-2170, 1981, pp. 387–408.

²⁵Croom, D. R., “Development of the Use of Spoilers as Vortex Attenuators,” *NASA Symposium on Wake Vortex Minimization*, edited by A. Gessow, NASA SP-409, 1976, pp. 337–357.

²⁶Jacobsen, R. A., and Barber, M. R., “Flight-Test Techniques for Wake-Vortex Minimization,” *NASA Symposium on Wake Vortex Minimization*, edited by A. Gessow, NASA SP-409, 1976, pp. 191–217.

²⁷Patterson, J. C., and Jordan, F. L., Jr., “Thrust Augmented Attenuation,” *NASA Symposium on Wake Vortex Minimization*, edited by A. Gessow, NASA SP-409, 1976, pp. 258–274.

²⁸Stickle, J. W., and Kelly, M. W., “Ground-Based Facilities for Evaluating Vortex Minimization Concepts,” *NASA Symposium on Wake Vortex Minimization*, edited by A. Gessow, NASA SP-409, 1976, pp. 123–154.

²⁹Rossow, V. J., “Lift-Generated Vortex Wakes of Subsonic Transport Aircraft,” *Progress in Aerospace Sciences*, Vol. 35, No. 6, 1999, pp. 507–660.

³⁰Chevalier, H., “Flight Test Studies of the Formation and Dissipation of Trailing Vortices,” *Journal of Aircraft*, Vol. 10, No. 1, 1973, pp. 14–18.

A. Plotkin
Associate Editor